Journal of
Marine Science and Engineering

Article

Static Model of the Underwater Soft Bending Actuator Based on the Elliptic Integral Function

Ri Lin, Anzhe Yi, Mingwei Lin *, Canjun Yang and Zhuoyu Zhang

State Key Laboratory of Fluid Power and Mechatronic Systems, Zhejiang University, Hangzhou 310027, China; 11925004@zju.edu.cn (R.L.); 22025102@zju.edu.cn (A.Y.); ycj@zju.edu.cn (C.Y.); 12025022@zju.edu.cn (Z.Z.)
* Correspondence: lmw@zju.edu.cn; Tel.: +86-180-6068-2762

Abstract: Underwater soft manipulators are increasingly used for grasping underwater organisms and cultural relics due to their compliance and ability to protect delicate objects. Unlike rigid manipulators, these soft manipulators feature underwater soft bending actuators that deform under external forces, making their shape and output force challenging to predict. Consequently, classical beam theory is no longer applicable. To address these issues, this article models the underwater soft bending actuator as a cantilever beam and establishes its shape and output force using elliptic integral functions. Additionally, this article proposes a method for determining the unknown parameters of the driver shape and output force model using optimization techniques and introduces a solution process based on the particle swarm optimization framework. Given the role of tensile and bending stiffness in the actuator's performance, this paper employs a parameter identification method based on length and bending angle information. Tests demonstrate that the proposed method effectively estimates the deformation and output force of the underwater soft bending actuators, confirming its accuracy.

Keywords: soft actuators; soft robotics; static model; Euler–Bernoulli's beam; parameter identification

Citation: Lin, R.; Yi, A.; Lin, M.; Yang, C.; Zhang, Z. Static Model of the Underwater Soft Bending Actuator Based on the Elliptic Integral Function. *J. Mar. Sci. Eng.* **2024**, *12*, 1772. https://doi.org/10.3390/jmse12101772

Academic Editor: Rafael Morales

Received: 5 September 2024
Revised: 30 September 2024
Accepted: 2 October 2024
Published: 6 October 2024

1. Introduction

Traditional robotic arms, with their rigid contact during grasping, risk damaging the surface structure of delicate objects if the grasping force is not carefully controlled. This issue is particularly problematic when handling fragile items. In contrast, soft actuators make gentle contact with target objects and adapt to their surfaces, a feature that has drawn increasing scholarly interest. Their compliance and safety make soft actuators valuable for underwater applications [1–4]. In autonomous underwater vehicle (AUV) recovery, traditional rigid docking methods often result in impact forces that can affect the AUV's operational lifespan on the seabed [5–7]. Lin et al. proposed a soft docking system that uses underwater soft bending actuators to mitigate impact forces and expand the docking area [8]. Soft actuators have also become crucial for grasping underwater organisms. For instance, Gong et al. developed a flexible gripper for sea cucumbers, providing both effective grasping and protection [3]. Additionally, soft grippers are ideal for handling cultural relics like porcelain and glass, which are easily damaged by rigid robotic arms. Liu et al. created a soft gripper specifically for porcelain artifacts [9]. Soft actuators, including those driven by dielectric elastomers [10–12], shape memory alloys [13], cables [14], electromagnetic mechanisms [15], and fluids [16,17]. Cable- and fluid-driven soft actuators are commonly used due to their ability to generate significant forces [18]. Among these, fluid-driven actuators are particularly suited for underwater environments. Based on the aforementioned applications, it is evident that many soft actuators possess elongated structures and a substantial range of motion, making them well-suited for object transport [19–21]. Concurrently, a flexible actuator must generate a sufficient output force to effectively grasp the target object. Consequently, accurately estimating the morphological changes and output forces of flexible actuators is a critical research area that must be addressed in the practical application of these drives.

Many scholars have modeled and analyzed the shape changes and output forces of soft actuators, and the most commonly used soft actuator model is the constant curvature model. Benjamin et al. proposed a constant curvature model based on Euler–Bernoulli beams for designing and optimizing soft fluid actuators [21]. Gursel et al. established a constant curvature analysis model to estimate the quasi-static bending displacement of soft actuators [22]. In addition, Zhong et al. proposed a constant curvature model to describe the deformation of soft pneumatic dexterous grippers [23]. Although soft actuators typically do not bend with a constant curvature, they can locally form a constant curvature, thus proposing the Piecewise Constant Curvature (PCC) method. Sadati et al. introduced a continuous soft arm analysis method based on PCC [24]. Alici et al. proposed a modeling method based on PCC to estimate the nonlinear bending of polymer actuators [25]. In addition, some scholars have modeled soft actuators based on the assumption of non-constant curvature, with the most common being the Cosserat method. Renda proposed a multi-stage flexible robotic arm model based on the Cosserat method and validated it through simulation and experiments [26]. Li et al. also proposed a method that combines the continuous Cosserat static model with the PCC method to derive the analytical formula of the model, which facilitates controller design [27]. In addition, other modeling methods have been proposed. For example, Liu et al. and Sachin et al. proposed an analytical model for calculating planar output force contact using finite strain membrane theory [28,29]. Dou et al. introduced a hybrid soft robot manipulator capable of controlling elongation and provided a modeling method based on balance principle and assumed prior deformation configuration [30]. However, the above two models are only applicable to the form of corrugated pipes. Fang et al. proposed a geometry based framework for calculating the deformation of flexible robots within the elastic range of linear materials [31]. The above method is suitable for situations where the load force is much smaller than its own driving force, which makes it difficult to apply in situations where large deformations occur under load. To address these issues, this paper proposes a static analysis model for soft actuators based on elliptic integral functions, aimed at estimating the shape and output force of soft actuators under multiple loads.

The structure of this article is as follows: the second part introduces the configuration of the underwater soft bending actuator used in this article. The Section 3 outlines the theoretical background of modeling using finite element iterative method, and the Section 4 introduces the model solution process based on particle swarm algorithm. The Section 5 introduces the tensile stiffness and bending stiffness identification method using the length and bending angle of the actuator. The Section 6 described the experiment and discussed the results. Finally, this article provides a summary in Section 6.

The contributions of this article are as follows:

(1) We proposed a calculation method based on the elliptic integral function capable of estimating the shape and output force of the underwater soft bending actuator;

(2) We proposed a method for determining the unknown parameters of the actuator's shape and output force model using an optimization method and introduced a solution process based on the particle swarm optimization framework;

(3) We developed an underwater testing environment for underwater soft bending actuator utilizing water drive and conducted experiments to estimate the shape and output force of the underwater soft bending actuator.

2. Configuration of the Underwater Soft Bending Actuator

To facilitate the study of underwater marine organisms, such as starfish and sea cucumbers, as well as artifacts, we designed an underwater collector that integrates an ROV with a soft gripper. This system is capable of landing on the seafloor to capture nearby target objects. The underwater soft bending actuator (USBA) serves as the most critical component of the soft gripper. The USBA depicted in Figure 1, developed in this article, is water-driven and designed for underwater environment. As water is injected into the internal chamber of the USBA, the pressure within the chamber steadily increases, thereby causing the USBA to bend. The manufacturing material for the USBA is silicone with a Shore hardness of 10, a 1:1 mixture of two silicone liquids, DP7508 (A) and DP7508 (B). The cured silicone on the USBA has a density of approximately $\rho_s = 1150\ \mathrm{kg/m^3}$, which is slightly larger than that of water.

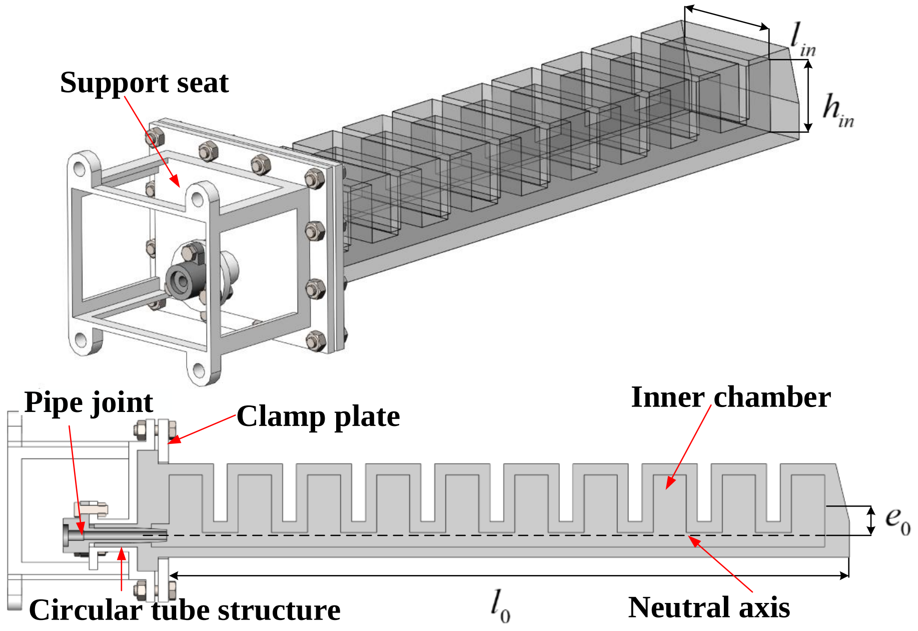

Figure 1. The structure of the USBA.

The base of the USBA is positioned between the 3D printed support seat and the clamp plate, secured in place with screws. Adjacent to the USBA's inlet is a circular tube structure crafted from poured silicone, housing a hydraulic pipe joint integrated on its inner surface. The outer diameter of the hydraulic pipe joint is marginally larger than the inner diameter of the circular silicone joint, ensuring pressure integrity through deformation induced by compression contact. As depicted in Figure 1, the dashed line represents the neutral axis of the bending deformation of the USBA. The rectangular surface located at the end of the actuator chamber withstands water pressure, with a length of l_{in} and a height of h_{in}. The distance from the center of the pressure-bearing surface in the vertical direction to the bending neutral axis is denoted as e_0, while the distance from the USBA's end to the clamp plate is l_0. The volume of the suspended soft actuator (excluding the liquid within the inner chamber) is represented by V.

3. Static Model of the USBA under Multiple Loads

When a USBA is subjected to internal driving pressure and external load, its shape undergoes changes. Failure to accurately establish the relationship between the shape change of the soft actuator and load will result in an inability to control the position and output force of the actuator. The existing static models in the literature are not effective at addressing this issue, prompting the proposal of a method for the static modeling of the USBA based on the elliptic integral function in this paper. Due to the corrugated structure of the USBA, its mass, bending stiffness, and tensile stiffness are not uniformly distributed along the axis. However, the USBA can be viewed as consisting of many discrete segments, each primarily exhibiting the characteristics of the central chamber. If we define the equivalent tensile strength and equivalent bending strength for a single segment, we can consider the entire USBA as being composed of multiple such segments uniformly distributed along its axis [22,25,28]. Under these assumptions, the actual deformation of the USBA is relatively small (less than 70%), allowing us to treat it as equivalent to a cantilever beam represented by its neutral axis [25]. The typical force state of a USBA under multiple loads is illustrated in Figure 2a. Considering that the USBA operates underwater and is influenced by both gravity and buoyancy, and given that the density of silicone rubber is slightly less than water's, the effects of gravity and buoyancy can be considered to cancel each other out. When water with pressure P_d is injected into the inner channel of the USBA, the effect of this pressure on the USBA can be equivalent to a force F_p and a bending moment M_p along the neutral axis direction, with their calculation expressions provided as:

$$\begin{aligned} F_p &= P_d A_{in} \\ M_p &= P_d A_{in} e_0 \end{aligned} \tag{1}$$

The area of water pressure at the end of the inner chamber, denoted as A_{in}, is equal to the product of l_{in} and h_{in}. Consequently, when subjected to driving pressure, the USBA extends along the neutral axis direction while also causing the neutral axis to bend. Furthermore, the end of the USBA sustains a force F at an angle φ_0 in the x-axis direction. As a result of the various loads mentioned above, the endpoint of the neutral axis undergoes a change in x_0 in the x-direction and y_0 in the y-direction. The length of the neutral axis becomes l_d, and the angle between the tangent direction of the end and the x-axis is denoted as θ_0.

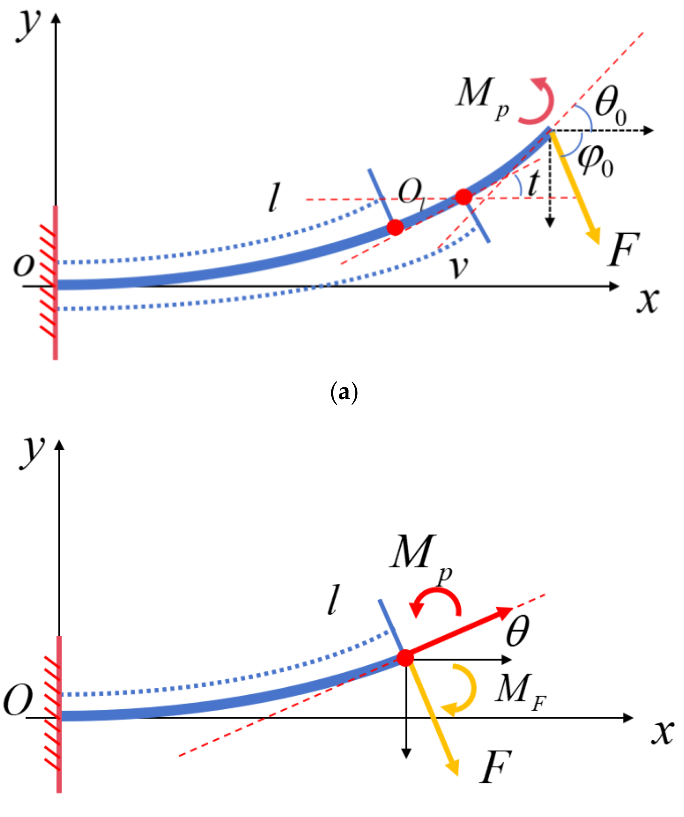

(**a**)

(**b**)

Figure 2. Equivalent Euler–Bernoulli cantilever beam model. (**a**) Analysis of typical multi-load conditions based on cantilever beams; (**b**) analysis of the force state of the point O_l. The yellow line with an arrow indicates the force exerted by the load. The yellow arc with arrows represents the bending moment resulting from the load. The red line with an arrow signifies the driving force, while the red arc with an arrow illustrates the bending moment caused by the driving force. The blue line represents the neutral axis of the USBA.

When the USBA undergoes deformation under the action of driving force, load force and deriving moment, it can be considered as a rigid body with corresponding shapes that achieves force balance at various points under the aforementioned force conditions. This rigid cantilever beam has a bending stiffness EI and a tensile stiffness EA. It is known that when a force $\vec{F}$ is applied to a point in a continuous object, its impact on another point at a distance of $\vec{r}$ from that point is equivalent to a parallel force $\vec{F}$ along with the bending moment $\vec{F} \times \vec{r}$. According to the above principles and force state shown in Figure 2b, the bending moment at any point O_l on the cantilever beam is:

$$M(l) = M_p - \int_l^{l_0} F \sin(\theta + \varphi_0) dl \tag{2}$$

The integral term is the bending moment generated by force F at that point O_l. According to the Euler–Bernoulli equation and the coordinates defined in the figure, the curvature K of this point is:

$$K = \frac{d\theta}{dl} = -\frac{M(l)}{EI} \tag{3}$$

Based on the above equation, it is clear that the presence of an external force F results in varying curvature at each point along the cantilever beam. Consequently, the deformed cantilever beam will not display a constant curvature arc shape. To further investigate the characteristics of the angle change rate, additional differentiation is carried out to obtain the following expression:

$$\frac{d^2\theta}{dl^2} = \frac{-F \sin(\theta + \varphi_0)}{EI} \tag{4}$$

Combining Formulas (2)–(4), it is obtained that

$$K\frac{dK}{d\theta} = \frac{-F \sin(t + \varphi_0)}{EI} \tag{5}$$

Formula (5) serves as the characteristic equation for the deformation of a cantilever beam. Assuming θ_0 denotes the bending angle at the end of the cantilever beam and M represents the driving moment, it follows from Formula (5) that:

$$\frac{K^2}{2} - \frac{1}{2}\left(\frac{M_p}{EI}\right)^2 = \frac{F}{EI}(-\cos(\theta + \varphi_0) + \cos(\theta_0 + \varphi_0)) \tag{6}$$

According to Formula (6), the curvature of any point on the cantilever beam can be determined as

$$K = \pm\sqrt{\frac{2F}{EI}}\sqrt{(\cos(\theta_0 + \varphi_0) - \cos(\theta + \varphi_0)) + \frac{M_p^2}{2FEI}} \tag{7}$$

In the application of USBA, there are typically two scenarios. In the first scenario, a constant gravity object is fixed at the end of the USBA. By applying pressure to the flow channel, the object can move freely to another position, which we define as the “end-free state”. In the second scenario, the USBA makes contact with a surface at a specified position due to applied pressure, generating a contact force that clamps the surface. This is defined as the “end constraint state”.

3.1. End-Free State

In this state, the end position of the USBA is not constrained, and its shape is determined by both the driving pressure and the load force. Based on the magnitude of the load force, the deformation of the USBA in this state can be categorized into the following two types:

(a) **The first type:** the curvature and the bending angle of any point on the neutral axis of the USBA are greater than 0, as shown in Figure 3a. In this state, the curvature on the cantilever beam is positive. By substituting the positive curvature in (8) into Formula (3) and integrating while considering the boundary conditions of the cantilever beam $(l = 0,\ \theta = 0)$, it is obtained that:

$$\int_0^l dl = \sqrt{\frac{EI}{2F}} \int_0^\theta \frac{dt}{\sqrt{(\cos(\theta_0+\varphi_0) - \cos(t+\varphi_0)) + \frac{M_p^2}{2FEI}}} \tag{8}$$

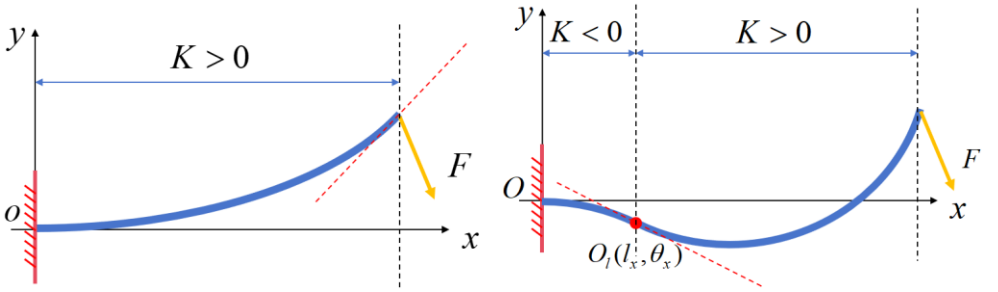

(**a**)

(**b**)

Figure 3. Two shape types of the deformed USBA. (**a**) There is no point on the USBA where *K* = 0. (**b**) There is a point on the USBA where *K* = 0.

Definition: $m = -\frac{2}{\frac{M_p^2}{2FEI} - 1 + \cos(\varphi_0+\theta_0)}$, and carry out transformation to the integral variable: $u = \frac{t+\varphi_0}{2}$. Formula (9) is then converted into the following expression:

$$\int_0^l dl = \sqrt{\frac{EI}{F}}\sqrt{-m}\left(\int_0^{\frac{\theta+\varphi_0}{2}} \frac{1}{\sqrt{1-m\sin^2(t)}}dt\right) - \sqrt{\frac{EI}{F}}\sqrt{-m}\left(\int_0^{\frac{\varphi_0}{2}} \frac{1}{\sqrt{1-m\sin^2(t)}}dt\right) \tag{9}$$

The two integral forms on the right side of the equation are typical of the first type of elliptic incomplete integrals. Therefore, we use the first-kind incomplete elliptic integral function to represent them:

$$l_d(\theta) = \sqrt{\frac{-mEI}{F}}\left(\alpha\left(\frac{\varphi_0+\theta}{2}, m\right) - \alpha\left(\frac{\varphi_0}{2}, m\right)\right) \tag{10}$$

According to the definition of elliptic function: if $l = F(\psi, m)$, then $\psi = am(l, m)$, where $am(\cdot)$ refers to the Jacobian elliptic amplitude function. Therefore, the bending angle of any point on the cantilever beam corresponding to that point is:

$$\theta = 2am\left(\sqrt{\frac{F}{-mEI}}(l(\theta) + \Delta l), m\right) - \varphi_0 \tag{11}$$

where $\Delta l = \sqrt{\frac{-mEI}{F}}\alpha\left(\frac{\varphi_0}{2}, m\right)$. In fact, describing the deformed cantilever beam's curve in Cartesian coordinates is also of interest to us:

$$\begin{aligned} y &= \int_0^{\theta}\sqrt{\frac{EI}{2F}}\frac{\sin t dt}{\sqrt{(\cos(\theta_0+\varphi_0)-\cos(t+\varphi_0))+\frac{M_p^2}{2FEI}}} = \cos\varphi_0 F_{\sin} - \sin\varphi_0 F_{\cos} \\ x &= \int_0^{\theta}\sqrt{\frac{EI}{2F}}\frac{\cos t dt}{\sqrt{(\cos(\theta_0+\varphi_0)-\cos(t+\varphi_0))+\frac{M_p^2}{2FEI}}} = \sin\varphi_0 F_{\sin} + \cos\varphi_0 F_{\cos} \end{aligned} \tag{12}$$

where the expression for $F_{\sin}$ is:

$$\begin{aligned} F_{\sin} &= \int_0^{\theta}\sqrt{\frac{EI}{2F}}\frac{\sin(t+\varphi_0)dt}{\sqrt{(\cos(\theta_0+\varphi_0)-\cos(t+\varphi_0))+\frac{M_p^2}{2FEI}}} \\ &= \sqrt{\frac{2EI}{F}}\left(\sqrt{\frac{2}{m}+1-\cos(\theta+\varphi_0)}-\sqrt{\frac{2}{m}+1-\cos(\varphi_0)}\right) \end{aligned} \tag{13}$$

And the expression for $F_{\cos}$ is:

$$F_{\cos} = \sqrt{\frac{EI}{2F}}\int_0^{\theta}\frac{\cos(t+\varphi_0)dt}{\sqrt{(\cos(\theta_0+\varphi_0)-\cos(t+\varphi_0))+\frac{M_p^2}{2FEI}}} \tag{14}$$

The integral function cannot directly obtain the original function. Define $m = -\frac{2}{\frac{M_p^2}{2FEI}-1+\cos(\varphi_0+\theta_0)}$ in the above integral equation and replace the integral variable with $u = \frac{t+\varphi_0}{2}$ to obtain the expression of $F_{\cos}$:

$$F_{\cos} = \sqrt{\frac{-mEI}{F}}\frac{m-2}{m}\int_{\frac{\varphi_0}{2}}^{\frac{t+\varphi_0}{2}}\frac{1}{\sqrt{1-m\ \sin^2 u}}du + \sqrt{\frac{-mEI}{F}}\frac{2}{m}\int_{\frac{\varphi_0}{2}}^{\frac{t+\varphi_0}{2}}\sqrt{1-m\ \sin^2 u}du \tag{15}$$

The second integral is a second-kind incomplete elliptic integral function $\beta(\cdot)$, where m is the modulus of the elliptic integral function. Therefore, $F_{\cos}$ can be expressed as:

$$F_{\cos} = \sqrt{\frac{-mEI}{F}}\frac{m-2}{m}\left(\alpha\left(\frac{\theta+\varphi_0}{2}\right)-\alpha\left(\frac{\varphi_0}{2}\right)\right) + \sqrt{\frac{-mEI}{F}}\frac{2}{m}\left(\beta\left(\frac{\theta+\varphi_0}{2}\right)-\beta\left(\frac{\varphi_0}{2}\right)\right) \tag{16}$$

In the force state shown in Figure 2b, the original length dl' near point O_l is stretched to dl, and the relationship between the two length is expressed as follows:

$$dl'(1+\varepsilon) = dl \tag{17}$$

According to the force state analysis in Figure 2b, the strain is:

$$\varepsilon = \frac{F\cos(\theta+\varphi_0)+F_p}{EA} \tag{18}$$

Combining Formulas (17) and (18) and integrating, the original length from point O_l to the root of the neutral axis is obtained as:

$$l'(\theta) = \sqrt{\frac{EI}{2F}}\int_0^{\theta}\frac{1}{1+\frac{F\cos(t+\varphi_0)+F_p}{EA}}\frac{dt}{\sqrt{(\cos(\theta_0+\varphi_0)-\cos(t+\varphi_0))+\frac{M_p^2}{2FEI}}} \tag{19}$$

Similarly, by defining $m = -\frac{2}{\frac{M_p^2}{2FEI} - 1 + \cos(\varphi_0 + \theta_0)}$ and $n = \frac{2F}{EA + F + F_p}$ in the above equation and replacing the integral variable with $u = \frac{t + \varphi_0}{2}$, it is obtained that:

$$l'(\theta) = \frac{nEA}{2F}\sqrt{\frac{-mEI}{F}}\int_{\frac{\varphi_0}{2}}^{\frac{\theta + \varphi_0}{2}} \frac{1}{1 - n\sin^2 u}\frac{du}{\sqrt{1 - m\sin^2 u}} \tag{20}$$

The integral equation on the right side of the above equation is a third-kind incomplete elliptic integral function, denoted as $\gamma(\cdot)$, so the original length corresponding to the cantilever beam is denoted as:

$$l'(\theta) = \frac{nEA}{2F}\sqrt{\frac{-mEI}{F}}\left(\gamma\left(n, \frac{\theta + \varphi_0}{2}, m\right) - \gamma\left(n, \frac{\varphi_0}{2}, m\right)\right) \tag{21}$$

Therefore, for a USBA with a total length of l_d after deformation, its corresponding calculated original length is $l'(\theta_0)$. In the derivation formulas above, the bending angle θ_0 at the end of the neutral axis is unknown, so it is necessary to determine this value by solving the following equation:

$$l_0 = l'(\theta_0) = \frac{nEA}{2F}\sqrt{\frac{-mEI}{F}}\left(\gamma\left(n, \frac{\theta_0 + \varphi_0}{2}, m\right) - \gamma\left(n, \frac{\varphi_0}{2}, m\right)\right) \tag{22}$$

where l_0 is the original length of the USBA. Given the typical nonlinearity of this equation system, Equation (22) is transformed into the following optimization problem for resolution:

$$\min : f = |l_d - l(\theta_0)| \tag{23}$$

Once the angle θ_0 is figure out, the length of the USBA after deformation can be obtained according to Formula (10), and the curve shape of the neutral axis can be calculated through Formulas (12), (13) and (15).

(b) **The second type:** there exists a point $O_l(l_x, \theta_x)$ where the curvature zero. The curvature K of the cantilever beam on the left of point O_l is less than 0, while the curvature K on the right of point O_l is greater than 0, as shown in Figure 3b.

If the curvature of point O_l is 0, according to Formula (7), the bending angle at point O_l meets this condition: $\theta' = a\cos\left(\cos(\theta_0 + \varphi_0) + \frac{M_p^2}{2FEI}\right) - \varphi_0$. For the left side of the point, the angle range of the cantilever beam is $(0, \theta')$, and for the right side, it is (θ', θ_0). Assuming that the deformed lengths of the cantilever beam are l_{d1} on the left side of the point and l_{d2} on the right side, the calculation formulas for l_{d1} and l_{d2} are expressed as follows:

$$\begin{gathered} l_{d1} = -\sqrt{\tfrac{-mEI}{F}}\left(\alpha\left(\tfrac{\varphi_0 + \theta'}{2}, m\right) - a\left(\tfrac{\varphi_0}{2}, m\right)\right) \\ l_{d2} = -\sqrt{\tfrac{-mEI}{F}}\left(\alpha\left(\tfrac{\varphi_0 + \theta'}{2}, m\right) - a\left(\tfrac{\varphi_0}{2}, m\right)\right) + \sqrt{\tfrac{-mEI}{F}}\left(\alpha\left(\tfrac{\varphi_0 + \theta_0}{2}, m\right) - a\left(\tfrac{\varphi_0}{2}, m\right)\right) \end{gathered} \tag{24}$$

According to Formula (21), the original lengths corresponding to these two segments are expressed as:

$$\begin{gathered} l'_1 = -\tfrac{nEA}{2F}\sqrt{\tfrac{-mEI}{F}}\left(\gamma\left(n, \tfrac{\theta' + \varphi_0}{2}, m\right) - \gamma\left(n, \tfrac{\varphi_0}{2}, m\right)\right) \\ l'_2 = -\tfrac{nEA}{2F}\sqrt{\tfrac{-mEI}{F}}\gamma\left(n, \tfrac{\theta' + \varphi_0}{2}, m\right) + \tfrac{nEA}{2F}\sqrt{\tfrac{-mEI}{F}}\gamma\left(n, \tfrac{\theta_0 + \varphi_0}{2}, m\right) \end{gathered} \tag{25}$$

Similarly, the unknown parameter θ_0 is solved through the optimization method:

$$\min : f = \left|l_0 - l'_1 - l'_2\right| \tag{26}$$

Since the neutral axis is divided into two sections, the shape of the neutral axis also needs to be calculated in two segments. For the left section, where $\theta \in (0, \theta')$ and $K < 0$, the x and y coordinates are obtained according to Formulas (12), (13) and (15). However, the curvature in this section is less than 0; the expressions for $F_{\sin}$ and $F_{\cos}$ are denoted as:

$$\begin{aligned} F_{\sin} &= -\sqrt{\tfrac{2EI}{F}}\left(\sqrt{\tfrac{2}{m}+1-\cos(\theta+\varphi_0)} - \sqrt{\tfrac{2}{m}+1-\cos(\varphi_0)}\right) \\ F_{\cos} &= -\sqrt{\tfrac{-mEI}{F}}\tfrac{m-2}{m}\left(\alpha\left(\tfrac{\theta+\varphi_0}{2}\right) - \alpha\left(\tfrac{\varphi_0}{2}\right)\right) - \sqrt{\tfrac{-mEI}{F}}\tfrac{2}{m}\left(\beta\left(\tfrac{\theta+\varphi_0}{2}\right) - \beta\left(\tfrac{\varphi_0}{2}\right)\right) \end{aligned} \tag{27}$$

According to Formulas (12) and (27), the coordinate of the point O_l is calculated as (x_{O_l}, y_{O_l}). For the right section, where $\theta \in (\theta', \theta_0)$, $K > 0$, the calculation method for x and y coordinates is:

$$\begin{aligned} y &= y^{*1} - y^{*2} + y_{O_l} \\ x &= x^{*1} - x^{*2} + x_{O_l} \end{aligned} \tag{28}$$

The calculation expressions for x^{*1}, y^{*1}, x^{*2}, and y^{*2} are:

$$\begin{aligned} y^{*1} &= \int_0^{\theta} \sqrt{\frac{EI}{2F}} \frac{\sin t dt}{\sqrt{(\cos(\theta_0+\varphi_0) - \cos(t+\varphi_0)) + \dfrac{M_p^2}{2FEI}}} \\ y^{*2} &= \int_0^{\theta'} \sqrt{\frac{EI}{2F}} \frac{\sin t dt}{\sqrt{(\cos(\theta_0+\varphi_0) - \cos(t+\varphi_0)) + \dfrac{M_p^2}{2FEI}}} \\ x^{*1} &= \int_0^{\theta} \sqrt{\frac{EI}{2F}} \frac{\cos t dt}{\sqrt{(\cos(\theta_0+\varphi_0) - \cos(t+\varphi_0)) + \dfrac{M_p^2}{2FEI}}} \\ x^{*2} &= \int_0^{\theta'} \sqrt{\frac{EI}{2F}} \frac{\cos t dt}{\sqrt{(\cos(\theta_0+\varphi_0) - \cos(t+\varphi_0)) + \dfrac{M_p^2}{2FEI}}} \end{aligned} \tag{29}$$

Formula (29) can be computed using Formulas (12)–(14). By using these formulas, the deformation of the neutral axis of the USBA can be determined.

3.2. End-Constrained State

In this state, the USBA makes contact with a surface at a specific position on the object upon pressurization and bending, resulting in the application of contact force, as shown in Figure 4. When it comes to grasping tasks, the strength of the output force becomes pivotal, as it is essential for securely grasping the object. In this context, the output force magnitude in the above formula transitions into an unknown variable. In this case, the shape form of the USBA is also the same as the end-free state as shown in Figure 2. The shape calculation method of the cantilever beam under two different forms has been derived in the section of end-free state, so the displacement y of the end on the y-axis can be calculated. In the scenario of end constraint state, the magnitude of the force acting on the end is unknown, so there are two unknown variables in the above formula: the bending angle θ_0 and output force F of the end. By solving the following system of equations, the values of these two unknowns can be determined.

$$\begin{cases} l(\theta_0) = l_0 \\ y_0 = \Delta y \end{cases} \tag{30}$$

Similarly, the system of equations is transformed into the following optimization problem for solution:

$$\min : f = |l_d - l_0| + |y_0 - \Delta y| \tag{31}$$

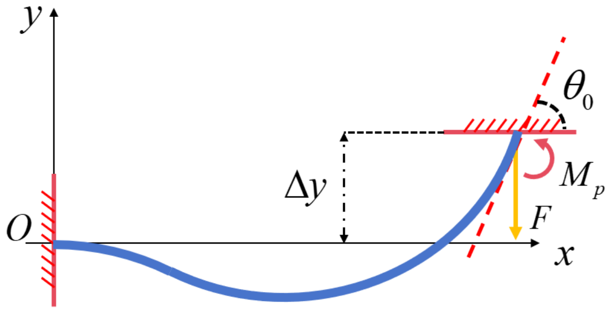

Figure 4. Analysis of the force state of the USBA when the endpoint is constrained.

4. Particle Swarm Optimization Algorithm-Based Solution Process for the Shape and Output Force of the USBA

In Section 3, we analyzed two typical states in the application of the USBA: the end-free state and the end-constrained state. Each scenario involves a different number of unknown parameters that need to be resolved. To accurately estimate the shape or output force of the USBA, it is essential to solve for these unknown parameters within the model. This article presents a solution process based on the standard particle swarm optimization framework for both types of scenarios, as illustrated in Figure 5.

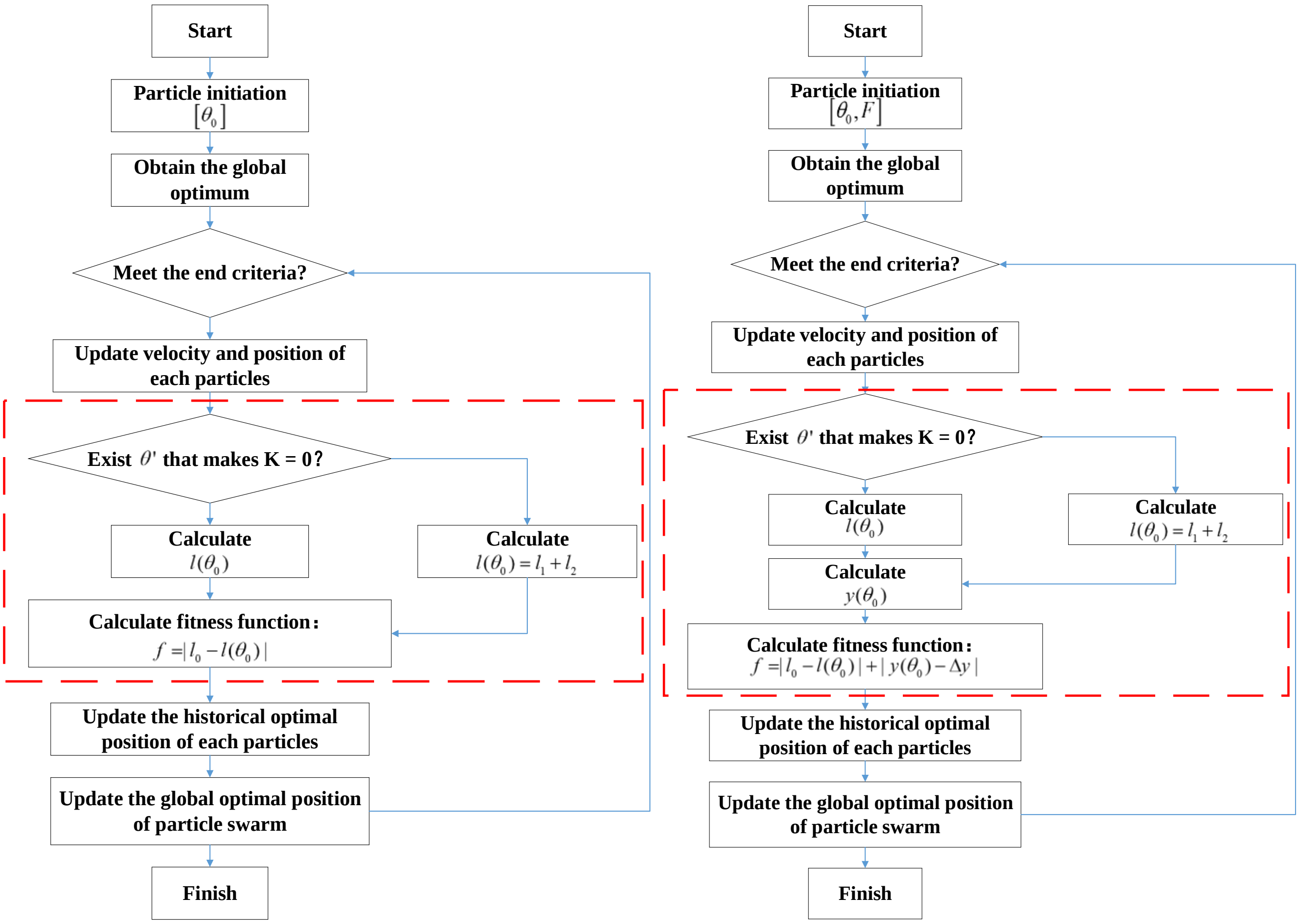

(**a**) (**b**)

Figure 5. The model solution framework. (**a**) Solution framework for "end-free state"; (**b**) solution framework for "end-constrained state". The content within the red dashed box has been modified to align with the actual model.

Figure 5a shows the process of solving the shape of the USBA under the load force and driving pressure in the end-free state. Since the unknown variable in this model is only the bending angle in the end, only one group of particle swarm representing this angle is set in the particle initialization. The content within the red dashed line is the modified part based on the model in this article. Firstly, according to the parameter information carried by the particles, it is determined whether there are points with curvature of 0 on the USBA. If not, the initial length value of the USBA can be directly calculated using Formula (20); if it exists, the USBA will be divided into two sections to calculate their respective initial length values, and the sum of them will be the initial length value calculated by the model. Next, the fitness function is calculated; if the value of fitness function is less than the finishing condition of the process (set at 0.0001 in this article), the particle update process is terminated; otherwise, the parameters carried by the particle swarm will be continuously optimized and updated until the number of iterations exceeds the set value (set at 10,000 in this article); it is determined that there is no solution in this state. Figure 5b shows the solution process of the USBA in the end-constrained state, which is roughly the same as that in the end-free state. There are two groups of particle swarm in this process, each group carrying the bending angle and output force of the end. In the red box, the algorithm first determines whether the USBA is divided into two segments for calculation based on the angle parameters carried by the particles, and then calculates the initial length of the USBA. In addition, it is necessary to calculate the displacement of the end in y-direction. Finally, the fitness function is calculated, and when the value is less than the set value (0.001), the iteration process ends. When the number of iterations exceeds the set value (1000), it is considered that there is no solution in the current state.

5. Parameter Identification of the USBA

To effectively utilize the method proposed in Section 7, it is essential to acquire the tensile stiffness EA and bending stiffness EI of the USBA beforehand. This article intends to solve these two parameters of soft actuators through system identification methods. In Figure 1, in the absence of an external load F and without considering the effects of gravity and buoyancy, the tension and bending of the soft actuator are solely generated by its own driving pressure. Hence, according to the Euler–Bernoulli equation, the bending curvature K of the soft actuator is given by:

$$K = \frac{1}{R} = \frac{P_d A_{in} e_0}{EI} \tag{32}$$

where R represents the bending radius of the USBA. Under this condition, the curvature of the USBA remains constant, resulting in the equivalent cantilever beam curve taking the form of a circular arc. The curvature of this arc can be determined from the bending angle θ and length l_d of the USBA:

$$K = \frac{\theta}{l_d} \tag{33}$$

The strain ε along the neutral axis of the USBA is related to the driving pressure as follows:

$$\varepsilon = \frac{P_d A_{in}}{EA} \tag{34}$$

The strain ε is obtained from the length after stretching:

$$\varepsilon = \frac{l_d - l_0}{l_0} \tag{35}$$

Based on the formula above, the bending stiffness and tensile stiffness can be determined by measuring the bending angle and length of the USBA after deformation. In the process of parameter identification, multiple sets of driving pressure, corresponding deformed length and bending angle data are sampled. Considering that the deformation of the USBA during the pressurization process is not very large, the tensile stiffness and bending stiffness of the USBA usually remain unchanged. According to Formulas (32) and (33), on the curvature–pressure curve graph, if a straight line with a slope of k_b can be fitted, then the bending stiffness is expressed as:

$$EI = (k_b / A_{in} e_0)^{-1} \tag{36}$$

Similarly, according to Formulas (34) and (35), if a straight line with a slope of k_e can be fitted on the strain–pressure curve graph, then the tensile stiffness is expressed as:

$$EA = (k_e / A_{in})^{-1} \tag{37}$$

6. Experiment Result and Discussion

As shown in Figure 6, the USBA is tested in a water cylinder with dimensions of 1000 mm × 500 mm × 600 mm. During the experiment, a gear pump is utilized to generate water pressure that drives the USBA. An electromagnetic switching valve positioned between the USBA and the gear pump is employed to regulate the pressure entering the internal chamber of the soft actuator. The pressure within the inner chamber is measured using a pressure gauge with an accuracy of 0.25 kPa. Additionally, the USBA is photographed using a camera with coordinate paper as the background, and the position of the neutral axis end is recorded. The length and bending angle of the deformed USBA are calculated through post-processing visual processing algorithms. The structural parameters of the USBA are outlined in Table 1.

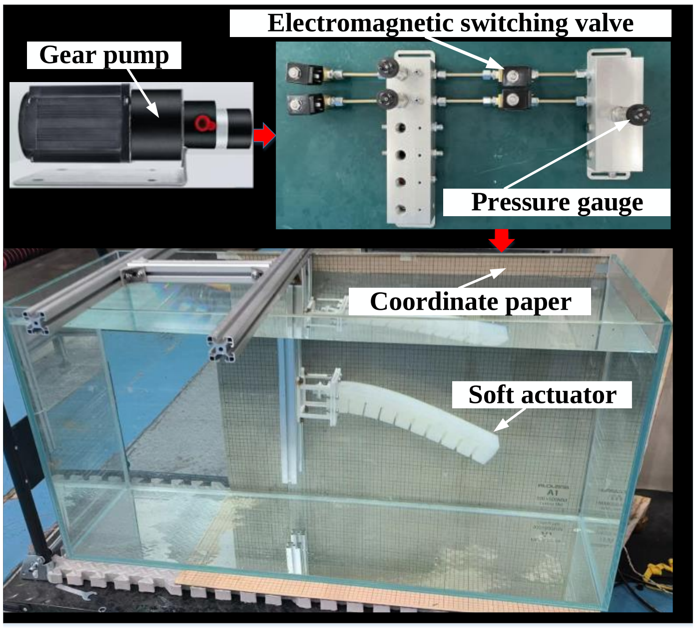

Figure 6. The test platform of the USBA.

Table 1. The parameter of the USBA.

Parameter	Value
l_0	394 mm
e_0	14.3 mm
$A_{in}(l_{in} \times h_{in})$	2668 mm^2 (64 mm × 42 mm)
ρ	1150 kg/m^3

6.1. Parameter Identification

Before conducting the analysis of deformation soft actuators using the proposed method based on the elliptic integral function, it is essential to ascertain the tensile stiffness and bending stiffness of the USBA. To accurately determine these parameters, the USBA is positioned as depicted in Figure 7a, with its bending plane perpendicular to the vertical plane. In this setup, the bending angle of the USBA in the bending plane remains unaffected by gravity and buoyancy. Various pressures are applied to the USBA, and the tensile stiffness (EA) and bending stiffness (EI) of the USBA are identified through measurements of the length and bending angle of the neutral axis of the USBA. The red dots in Figure 7b represent the measured coordinates of the endpoints under different driving pressures. The calculated strain shows a linear increase with the rising pressure, as depicted in Figure 7c. Consequently, the tensile stiffness of the USBA remains essentially constant during the bending process. Similarly, Figure 7d illustrates that the change in curvature K and the increase in pressure p exhibit a linear growth trend during the deformation process of the USBA, indicating that the bending stiffness EI also maintains a constant value. Subsequently, based on the collected data, the obtained values for the tensile and bending stiffness of the USBA are 308.6 N and 0.0806 N·m^2, respectively. Utilizing the estimated tensile stiffness and bending stiffness data, the coordinates of the USBA endpoints under different driving pressures are depicted in Figure 7b. The endpoints of the USBA calculated using the identified tensile and bending stiffness are consistent with the measured results, with an average position error of 8.1 mm.

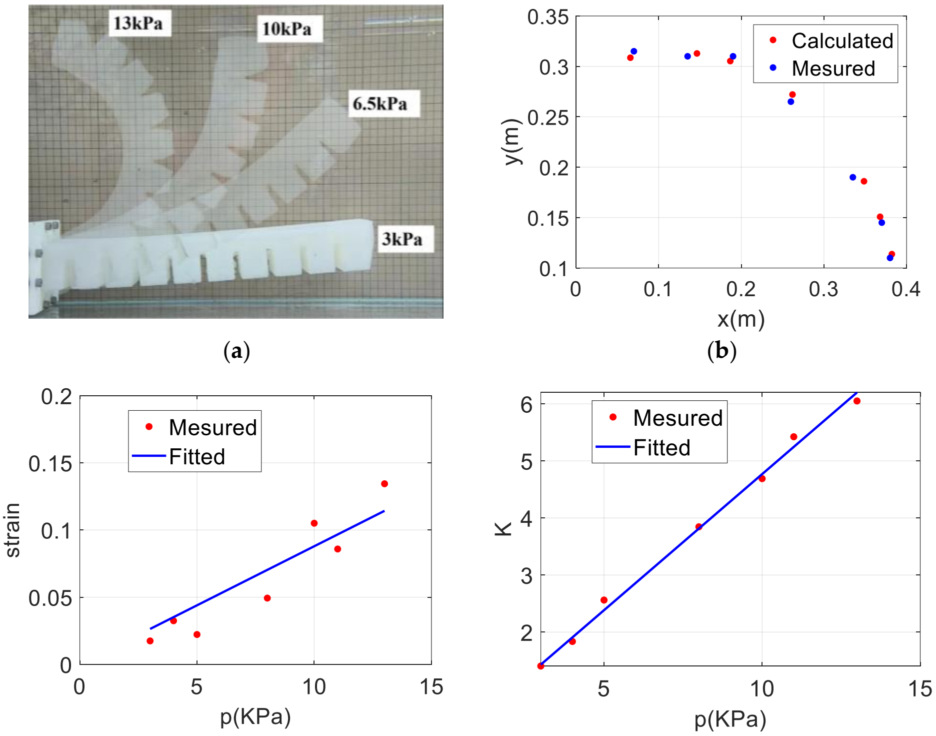

(**a**) (**b**)

(**c**) (**d**)

Figure 7. Tensile stiffness and bending stiffness identification results. (**a**) Identification test process; (**b**) the endpoint position measured and estimated by the proposed method; (**c**) the strain varies with driving pressure; (**d**) the curvature varies with driving pressure.

6.2. Shape and Position Estimation of the USBA

After obtaining the tensile and bending stiffness of the USBA, it becomes feasible to estimate the shape changes under load and the output force of the USBA. The solution framework for "end-free state" was utilized in this experiment. As illustrated in Figure 8, the USBA is bent on a vertical plane, bearing the weight generated by the counterweight at the end of the USBA, in addition to its own driving force, gravity and buoyancy. During the experiment, two different counterweights of 50 g and 100 g were applied to the end of the USBA. The effectiveness of the proposed model was verified by measuring the coordinates of the endpoints of the USBA under different driving pressures and loads, as well as the shape curve of the neutral axis. Figure 9 displays the shape of the USBA corresponding to different driving pressures under various end loading conditions. Notably, as the counterweight increases, the driving force required to reach the same position also increases. When the position of the endpoint of the USBA on the y-axis exceeds zero, the sensitivity of the shape change to input pressure increases with a larger counterweight. Figure 10 presents a comparison between the endpoint position coordinates of the USBA estimated by the proposed method for different counterweight conditions and the measured values under different test pressures. The change trend of the endpoint in the model calculation results aligns closely with that in the measured data. The average estimated errors for the endpoint position of the soft actuator under these two counterweights are 21.4 mm (50 g) and 22.1 mm (100 g), respectively. The error between the calculated endpoint positions corresponding to different driving pressures and the measured data under various counterweights is depicted in Figure 11, revealing a decreasing trend in the position calculation error with the increase in driving pressure. Notably, when the driving pressure exceeds 7 kPa, the position error in all counterweight states can be less than 20 mm. To verify whether the estimated shape of the soft actuator by the proposed metho matches the actual situation, a comparison was made between the neutral axis curve calculated by the proposed method and the actual shape image of the USBA. As shown in Figure 12, the neutral axis curve calculated by the model aligns well with the shape of the USBA. Based on the test results, it can be concluded that the proposed method effectively estimates the shape and endpoint of the USBA under different load conditions.

To demonstrate the superiority of the proposed model for USBA shape estimation, we compared it with the end coordinate estimated from classical beam theory (CBT) and the PCC models. Figure 13a,b display the estimated end coordinate values for the two models under load forces of 50 g and 100 g, respectively. Figure 13c illustrates the error between the estimated and measured end coordinate values of the USBA for both models. By comparing Figures 11 and 13, it is evident that the method proposed in this paper provides more accurate estimates of the end coordinate values. For a load of 50 g, the average error estimated by CBT is 116.2 mm, while the PCC method yields an average error of 63.5 mm. When the load increases to 100 g, the average error for CBT is 94 mm, and for the PCC method, it is 82.8 mm. In contrast, the proposed method demonstrates a lower average estimation error across both load conditions.

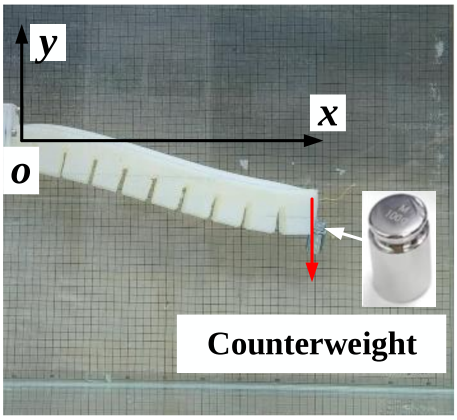

Figure 8. Schematic illustration of the end-bearing test scene.

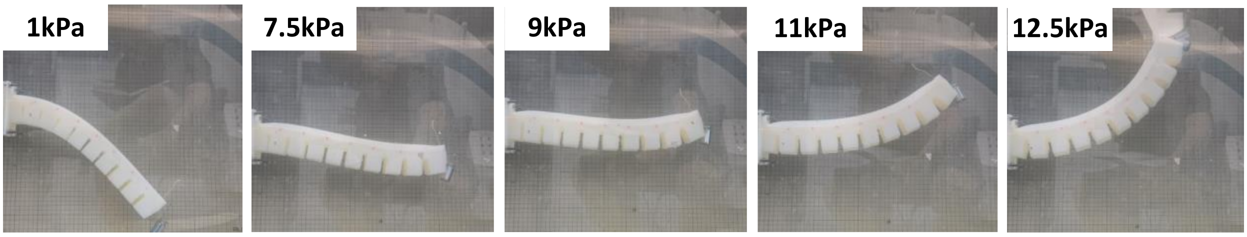

(a) weight=50g

(b) weight=100g

Figure 9. The shape of the USBA changes with driving pressure under different counterweights.

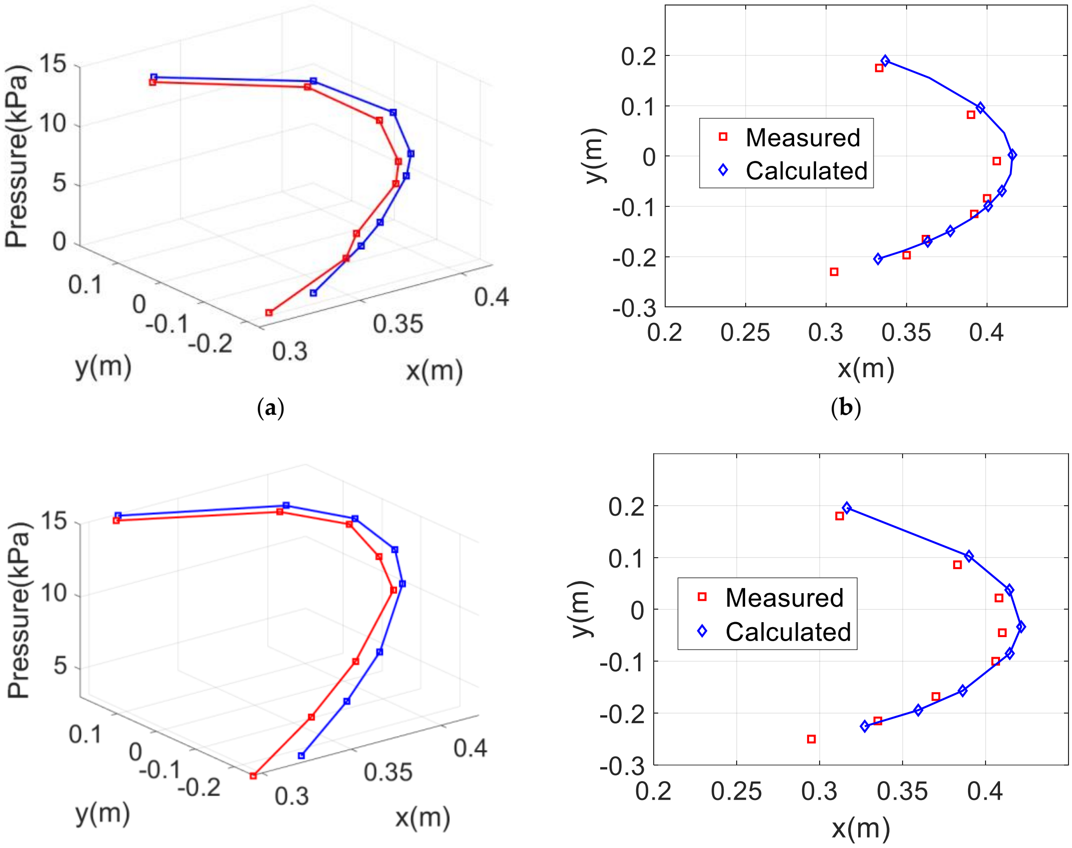

(**a**) (**b**)

(**c**) (**d**)

Figure 10. Comparison of the measured endpoint of the USBA with the estimated by the proposed method. (**a**) Endpoint varies with the driving pressure (weight = 50 g; red: measured; blue: estimated); (**b**) coordinate of the endpoints (weight = 50 g); (**c**) endpoint varies with the driving pressure (weight = 100 g; red: measured; blue: estimated); (**d**) coordinate of the endpoints (weight = 100 g).

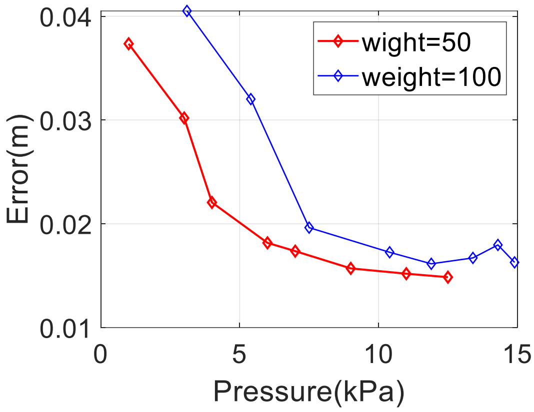

Figure 11. The position error between the measured and estimated.

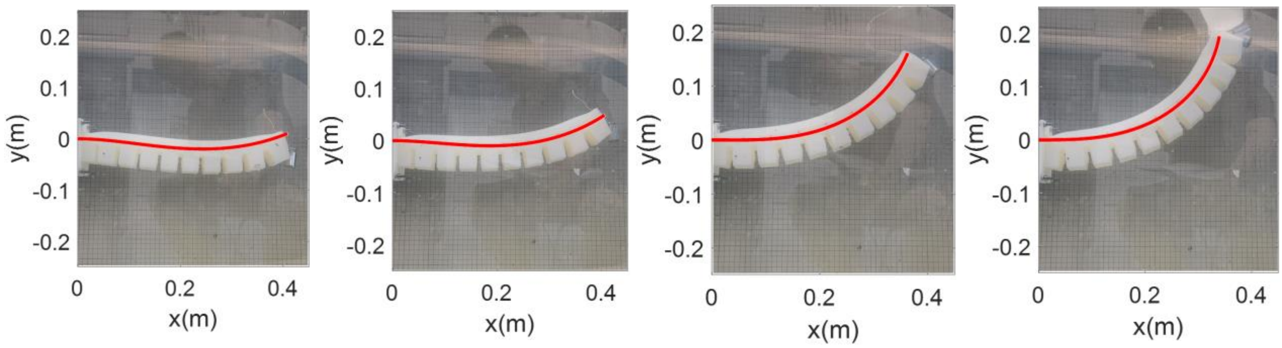

(**a**) 7.5 kPa (**b**) 9.25 kPa (**c**) 11.5 kPa (**d**) 12.5 kPa

Figure 12. Comparison between the deformation of the USBA estimated by the proposed method and the actual situation.

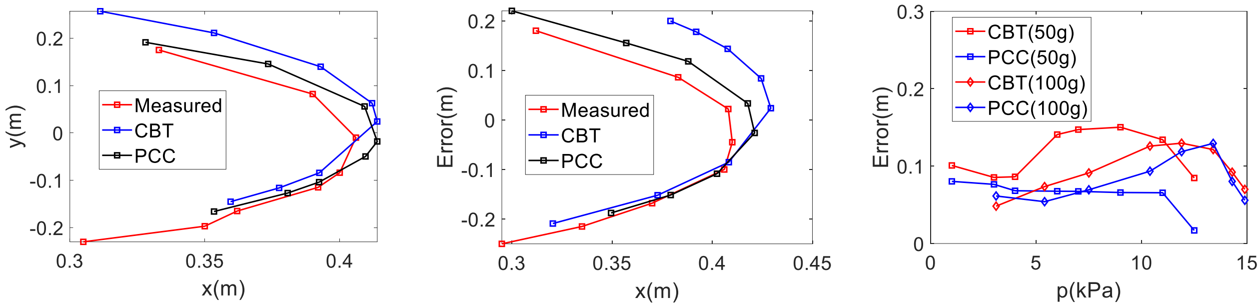

(**a**) (**b**) (**c**)

Figure 13. Performance of the CBT and PCC models in estimating the USBA endpoints. (**a**) Coordinate of the endpoints (weight = 50 g); (**b**) coordinate of the endpoints (weight = 100 g); (**c**) estimating error.

6.3. Output Force Estimation of the USBA

In this experiment, an underwater electronic scale with an accuracy of 1 g was positioned horizontally beneath the soft actuator to measure the output force at the end, as depicted in Figure 14. Owing to the smooth surface of the electronic scale in water, the USBA solely applies vertical pressure on the scale. Two different scenarios om which $\Delta y = 40$ mm and $\Delta y = 80$ mm were tested during the experiment, and Figure 15 illustrates the progression of the USBA's shape with increasing pressure in these two situations. The solution framework for "end-constrained state" was utilized in this experiment. According to the proposed method, the output force of the USBA exhibits a linearly increasing trend with the rise in driving pressure. The actual test results also demonstrate a linear increase in the output force of the soft actuator with the elevation of driving pressure, as depicted in Figure 16a. It is demonstrated in Figure 16b that the error in the estimated output force exhibits a significant decrease as the driving pressure increases. Specifically, when $\Delta y = 40$ mm and the driving pressure is greater than 10 kPa, the relative error of the model output force is less than 5% and continues to decrease. When $\Delta y = 80$ mm and the driving pressure is greater than 10 kPa, the relative error of the model output force is less than 8% and continues to decrease. In testing the USBA and planar contact force, we are interested not only in the magnitude of the contact force but also in the contact angle between the USBA and the planar contact point. As shown in Figure 16c, as the distance between the contact surface and the USBA increases, the contact angle also increases under the same driving pressure. While the release angle does not exhibit a completely linear increase with pressure, the trend of the increasing contact angle becomes more pronounced as the pressure rises. Additionally, as the pressure increases, the discrepancy between the estimated values calculated using the model presented in this article and the actual measured values gradually decreases (as shown in Figure 16d). Figure 17 demonstrates that during the output force test, the shape curve of the neutral axis estimated by the proposed model closely aligns with the shape change of the USBA in Figure 15, indicating the model's effectiveness in estimating both the shape change and the output force of the USBA.

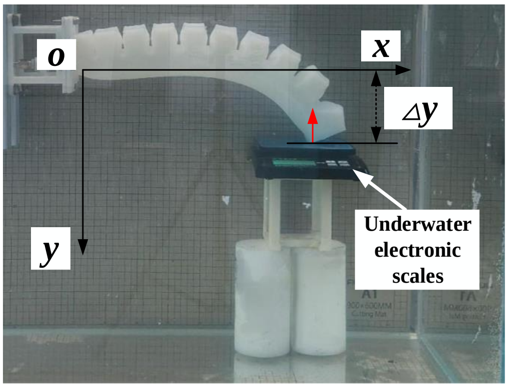

Figure 14. Schematic illustration of the output force test.

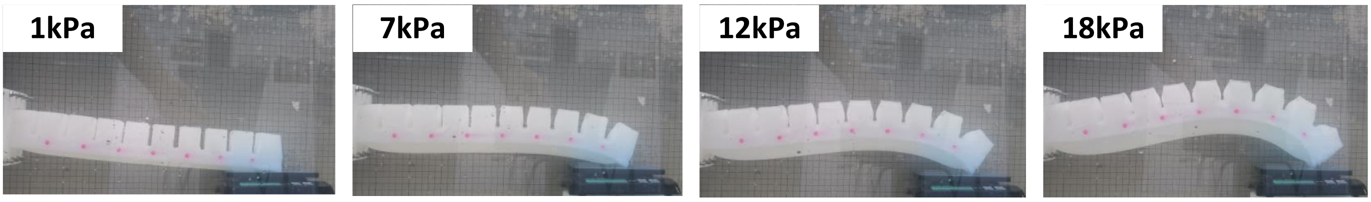

(**a**) Δy = 40 mm

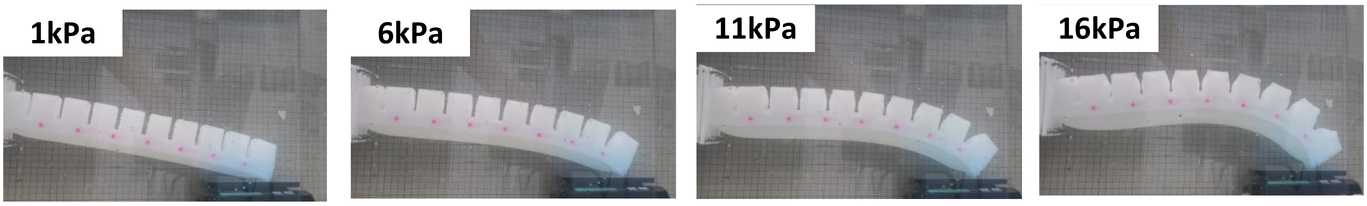

(**b**) Δy = 80 mm

Figure 15. The shape of the USBA varies with the driving pressure.

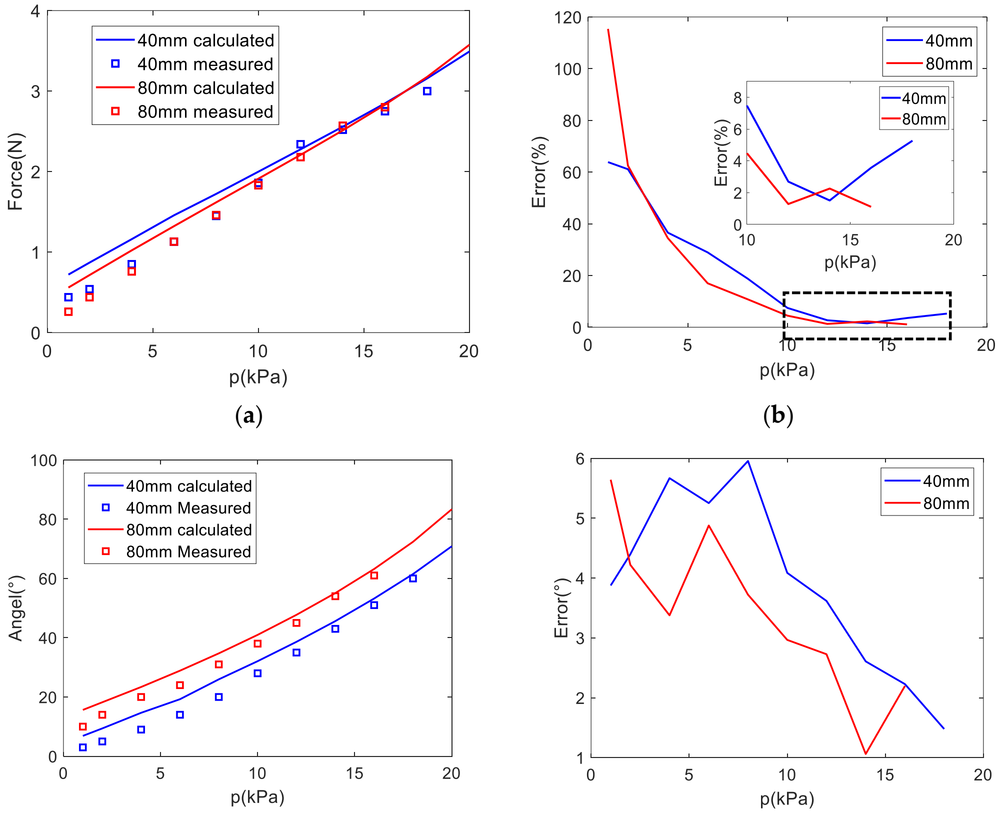

(**a**) (**b**)

(**c**) (**d**)

Figure 16. Comparison of the measured and theoretical values of the output force of the USBA. (**a**) The measured output force and the estimated force by the proposed method; (**b**) the relative error of the output force estimated with the driving pressure. (**c**) the measured and the estimated contacting angle of the endpoint; (**d**) the relative error of the estimated and the measured contacting angle of the endpoint vary with the driving pressure, Δy = 80 mm.

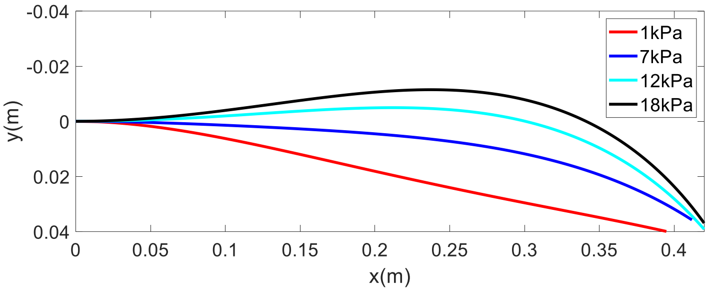

(**a**) Δy = 40 mm

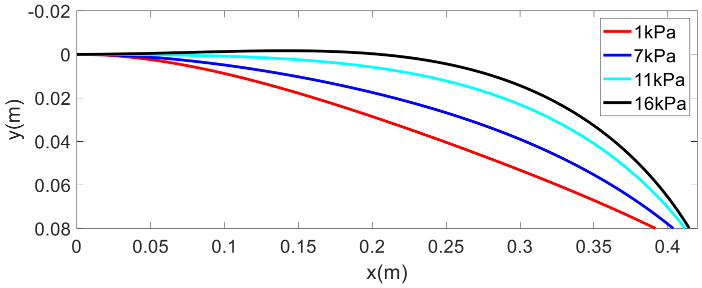

(**b**) Δy = 80 mm

Figure 17. The shape of the USBA changes with the driving pressure after contact with the plane.

To demonstrate the effectiveness of the proposed model in estimating output force, we compared it with the output force estimated by CBT and PCC model. Figure 18a,b show a comparison of the output force values estimated by various models against actual measured values under conditions of Δy = 40 mm and Δy = 80 mm, respectively. As shown in Figure 18, it is clear that the proposed method yields output force estimates that are closest to the actual measured values, followed by the estimates from the PCC model. This result further highlights the advantages of the proposed method in output force estimation.

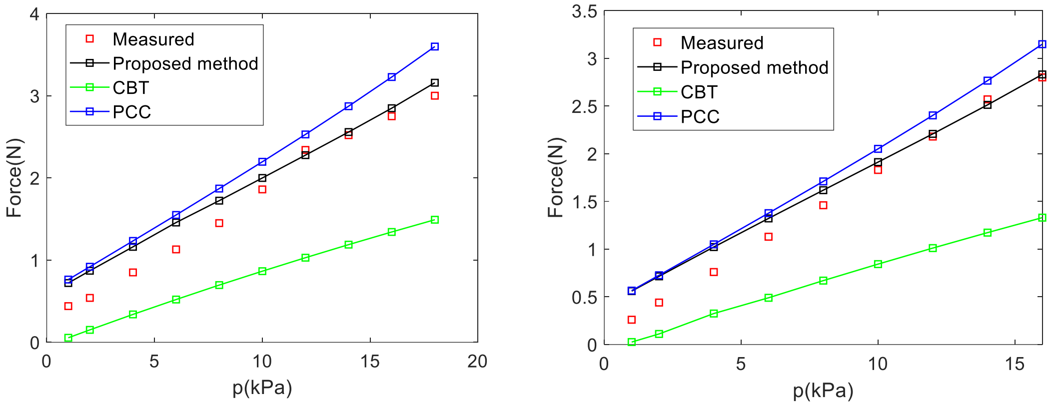

(**a**) Δy = 40 mm (**b**) Δy = 80 mm

Figure 18. Comparison of the effectiveness of the three output force calculation methods.

7. Conclusions

Soft actuators are increasingly replacing rigid actuators in numerous applications. However, there is currently a lack of reliable static models for describing the shape and output force of the soft actuator under large deformation scenarios. Therefore, this article proposes a calculation model based on the elliptic integral function for underwater soft bending actuators (USBAs) to estimate the deformation and output force. Moreover, this paper proposes a calculation process based on the particle swarm algorithm to figure out the unknown parameters in the proposed model. The method necessitates obtaining prior knowledge of tensile and bending stiffness; hence, this paper introduces a method for identifying tensile and bending stiffness of the USBA. The underwater test results demonstrate that the model can accurately estimate the end position and shape changes of the USBA under various loads, as well as the output force of the USBA acting on the contacting surface, thereby confirming the effectiveness of the model proposed.

In the future, our focus will be on exploring dynamic models and control methods for the USBA to achieve rapid and precise control under multi-load conditions.

Author Contributions: Conceptualization, R.L.; methodology, R.L. and M.L.; software, R.L. and Z.Z.; validation, R.L. and A.Y.; formal analysis, R.L.; investigation, M.L.; data curation, R.L. and A.Y.; writing—original draft preparation, R.L.; writing—review and editing, M.L.; supervision, C.Y.; project administration, C.Y.; funding acquisition, M.L. All authors have read and agreed to the published version of the manuscript.

Funding: This research was funded in part by the China Postdoctoral Science Foundation (2023M733072), National Natural Science Foundation of China (52101404) and Natural Science Foundation of Zhejiang Province (LY23E090002).

Institutional Review Board Statement: Not applicable.

Informed Consent Statement: Not applicable.

Data Availability Statement: Data is analyzed in this study.

Conflicts of Interest: The authors declare no conflicts of interest.

References

1. Jones, T.J.; Jambon-Puillet, E.; Marthelot, J.; Brun, P.-T. Bubble casting soft robotics. *Nature* **2021**, *599*, 229–233. [CrossRef]
2. Phillips, B.T.; Becker, K.P.; Kurumaya, S.; Galloway, K.C.; Whittredge, G.; Vogt, D.M.; Teeple, C.B.; Rosen, M.H.; Pieribone, V.A.; Gruber, D.F.; et al. A Dexterous, Glove-Based Teleoperable Low-Power Soft Robotic Arm for Delicate Deep-Sea Biological Exploration. *Sci. Rep.* **2018**, *8*, 14779. [CrossRef]
3. Gong, Z.; Fang, X.; Chen, X.; Cheng, J.; Xie, Z.; Liu, J.; Chen, B.; Yang, H.; Kong, S.; Hao, Y.; et al. A soft manipulator for efficient delicate grasping in shallow water: Modeling, control, and real-world experiments. *Int. J. Robot. Res.* **2021**, *40*, 449–469. [CrossRef]
4. Galloway, K.C.; Becker, K.P.; Phillips, B.; Kirby, J.; Licht, S.; Tchernov, D.; Wood, R.J.; Gruber, D.F. Soft Robotic Grippers for Biological Sampling on Deep Reefs. *Soft Robot.* **2016**, *3*, 23–33. [CrossRef] [PubMed]
5. Lin, M.; Lin, R.; Li, D.; Yang, C. Light Beacon-Aided AUV Electromagnetic Localization for Landing on a Planar Docking Station. *IEEE J. Ocean. Eng.* **2023**, *48*, 677–688. [CrossRef]
6. Lin, M.; Lin, R.; Yang, C.; Li, D.; Zhang, Z.; Zhao, Y.; Ding, W. Docking to an underwater suspended charging station: Systematic design and experimental tests. *Ocean Eng.* **2022**, *249*, 110766. [CrossRef]
7. Lin, M.; Yang, C. Ocean Observation Technologies: A Review. *Chin. J. Mech. Eng.* **2020**, *33*, 32. [CrossRef]
8. Lin, M.; Yi, A.; Lin, R.; Wu, X.; He, B.; Zhang, B.; Yang, C. Underwater fluid-driven soft dock for dynamic recovery of AUVs with improved pose tolerance. *Ocean Eng.* **2024**, *309*, 118466. [CrossRef]
9. Liu, J.; Iacaponi, S.; Laschi, C.; Wen, L.; Calistri, M. Underwater Mobile Manipulation: A Soft Arm on a Benthic Legged Robot. *IEEE Robot. Autom. Mag.* **2020**, *27*, 12–26.
10. Wang, X.; Mitchell, S.K.; Rumley, E.H.; Rothemund, P.; Keplinger, C. High-Strain Peano-HASEL Actuators. *Adv. Funct. Mater.* **2020**, *30*, 1908821. [CrossRef]
11. Rosset, S.; A Araromi, O.; Shintake, J.; Shea, H.R. Model and design of dielectric elastomer minimum energy structures. *Smart Mater. Struct.* **2014**, *23*, 085021. [CrossRef]
12. Araromi, O.; Conn, A.; Ling, C.; Rossiter, J.; Vaidyanathan, R.; Burgess, S. Spray deposited multilayered dielectric elastomer actuators. *Sens. Actuators A Phys.* **2011**, *167*, 459–467. [CrossRef]
13. Laschi, C.; Mazzolai, B.; Cianchetti, M. Soft robotics: Technologies and systems pushing the boundaries of robot abilities. *Sci. Robot.* **2016**, *1*, eaah3690. [CrossRef] [PubMed]
14. Dong, X.; Palmer, D.; Axinte, D.; Kell, J. In-situ repair/maintenance with a continuum robotic machine tool in confined space. *J. Manuf. Process.* **2019**, *38*, 313–318. [CrossRef]
15. Kim, Y.; Parada, G.A.; Liu, S.; Zhao, X. Ferromagnetic soft continuum robots. *Sci. Robot.* **2019**, *4*, eaax7329. [CrossRef] [PubMed]
16. Jiang, H.; Wang, Z.; Jin, Y.; Chen, X.; Li, P.; Gan, Y.; Lin, S.; Chen, X. Hierarchical control of soft manipulators towards unstructured interactions. *Int. J. Robot. Res.* **2021**, *40*, 411–434. [CrossRef]
17. Yan, J.; Zhang, X.; Xu, B.; Zhao, J. A New Spiral-Type Inflatable Pure Torsional Soft Actuator. *Soft Robot.* **2018**, *5*, 527–540. [CrossRef] [PubMed]
18. Chen, X.; Zhang, X.; Huang, Y.; Cao, L.; Liu, J. A review of soft manipulator research, applications, and opportunities. *J. Field Robot.* **2022**, *39*, 281–311. [CrossRef]
19. Jiao, Z.; Zhang, C.; Wang, W.; Pan, M.; Yang, H.; Zou, J. Advanced Artificial Muscle for Flexible Material-Based Reconfigurable Soft Robots. *Adv. Sci.* **2019**, *6*, 1901371. [CrossRef]
20. Quevedo-Moreno, D.; Roche, E.T. Design and Modeling of Fabric-Shelled Pneumatic Bending Soft Actuators. *IEEE Robot. Autom. Lett.* **2023**, *8*, 3110–3117. [CrossRef]
21. Gorissen, B.; Vincentie, W.; Al-Bender, F.; Reynaerts, D.; De Volder, M. Modeling and bonding-free fabrication of flexible fluidic microactuators with a bending motion. *J. Micromech. Microeng.* **2013**, *23*, 045012. [CrossRef]
22. Alici, G.; Canty, T.; Mutlu, R.; Hu, W.; Sencadas, V. Modeling and Experimental Evaluation of Bending Behavior of Soft Pneumatic Actuators Made of Discrete Actuation Chambers. *Soft Robot.* **2017**, *5*, 24–35. [CrossRef] [PubMed]
23. Zhong, G.; Hou, Y.; Dou, W. A soft pneumatic dexterous gripper with convertible grasping modes. *Int. J. Mech. Sci.* **2019**, *153–154*, 445–456. [CrossRef]
24. Sadati, S.M.H.; Shiva, A.; Ataka, A.; Naghibi, S.E.; Walker, I.D.; Althoefer, K.; Nanayakkara, T. A Geometry Deformation Model for Compound Continuum Manipulators with External Loading. In Proceedings of the 2016 IEEE International Conference on Robotics and Automation (ICRA), Stockholm, Sweden, 16–21 May 2016; pp. 4957–4962.
25. Alici, G. An effective modelling approach to estimate nonlinear bending behaviour of cantilever type conducting polymer actuators. *Sens. Actuators B Chem.* **2009**, *141*, 284–292. [CrossRef]
26. Renda, F.; Boyer, F.; Dias, J.; Seneviratne, L. Discrete Cosserat Approach for Multisection Soft Manipulator Dynamics. *IEEE Trans. Robot.* **2018**, *34*, 1518–1533. [CrossRef]
27. Li, H.; Xun, L.; Zheng, G.; Renda, F. Discrete Cosserat Static Model-Based Control of Soft Manipulator. *IEEE Robot. Autom. Lett.* **2023**, *8*, 1739–1746. [CrossRef]
28. Wang, Z.; Hirai, S. Analytical Modeling of a Soft Pneu-Net Actuator Subjected to Planar Tip Contact. *IEEE Trans. Robot.* **2022**, *38*, 2720–2733. [CrossRef]
29. Liu, Z.; Wang, F.; Liu, S.; Tian, Y.; Zhang, D. Modeling and Analysis of Soft Pneumatic Network Bending Actuators. *IEEE/ASME Trans. Mechatron.* **2021**, *26*, 2195–2203. [CrossRef]

30. Dou, W.; Zhong, G.; Yang, J.; Shen, J. Design and Modeling of a Hybrid Soft Robotic Manipulator with Compliant Mechanism. *IEEE Robot. Autom. Lett.* **2023**, *8*, 2301–2308. [CrossRef]
31. Fang, G.; Matte, C.-D.; Scharff, R.B.N.; Kwok, T.-H.; Wang, C.C.L. Kinematics of Soft Robots by Geometric Computing. *IEEE Trans. Robot.* **2020**, *36*, 1272–1286. [CrossRef]